STT-RAM MEMORY DEVICES

BY MONIKA ARORA, TOMMY MCKINNON, BRETT HEINRICH, EROL GIRT, CIARAN FOWLEY, EWA KOWALSKA, VOLKER SLUKA, AND ALINA MARIA DEAC

Over the past decades, the amount of digital information is increasing tenfold every five years. According to a report prepared by International Data Corporation (IDC) in 2014, the total amount of digital data generated globally will reach 44 ZB (1 ZB $=10^3$, EB $=10^6$, PB $=10^{12}$GB) by 2020 [1]. Hard drives are the most inexpensive devices used to store digital information that is infrequently accessed and stored for a long time. Hard drives, like magnetic tapes, have large storage capacity, however they are physically larger in size and slower in speed than the solid-state drives (SSD). Moreover, they have movable parts, which makes them more prone to damage and read/write errors.

As of now, there are three main types of solid-state semiconductor storage devices: static RAM (SRAM), dynamic RAM (DRAM), and flash memory. These are charge based solid-state electronic random access memories (RAMs) and each one of these has some merits and demerits. DRAM is being used as the main memory in all forms of modern computing devices. It is comprised of a single MOSFET (Metal-oxide semiconductor field-effect transistor) and a capacitor, which needs to be frequently refreshed as the capacitor leaks and the DRAM forgets its state. SRAM does not need to be refreshed. It is composed of 4–6 transistors, which makes SRAM much faster but requires more chip space. Flash memories have a very high density but comparatively low write speeds and endurance [2,3]. In this context, endurance means the number of read/write cycles a memory cell can go through before degradation occurs. Recently, in August 2015, Samsung introduced the world's largest solid state flash memory having 16TB storage capacity packed in a 2.5" case [4].

SUMMARY

The interaction between spin polarized current and local magnetic moment is studied in magnetic nanopillars for the use in future solid state STT-RAM memory devices.

The demand for improved memory has led to the emergence of new memory types. It was recently discovered that the interaction between the spin polarized current and the localized magnetic moment of a ferromagnet (FM) can induce magnetization reversal [5,6]. This effect is known as spin transfer torque (STT) and has been used to develop novel STT-RAM solid state memory devices. Spin transfer torque is mostly studied in nanopillars that consist of two ferromagnetic (FM) layers separated by a thin non-magnetic layer [6]. The first FM layer, the reference layer (RL), is used to create a spin-polarized current which then passes through the non-magnetic (NM) layer without a significant change in polarization and interacts with the second FM layer, the free layer (FL). This interaction exerts a spin torque on the magnetic moment of the free layer (FL) through a transfer of angular momentum from the polarized current to the FL magnetization. The device resistance depends on the relative orientation of the magnetic layers (parallel low resistance, and antiparallel high resistance), giving rise to giant magnetoresistance, GMR, if NM is metallic, or tunnel magnetoresistance, TMR, if NM is insulator [7–9]. If the polarized current density is large enough $>10^6$ A/cm^2, the spin torque will induce magnetization reversal in the FL [6].

STT-RAM is a non-volatile random-access magnetic memory (it retains its information when power is turned off) that suffers no degradation over time and has no moving parts [10]. It is also much faster than flash memory [11]. In STT-RAM, information is recorded by inducing magnetization reversal in the FL. GMR or TMR is then used to detect the magnetization direction of the FL [12,13]. In high frequency electronics impedance matching is extremely important. Although the signal for the GMR devices is smaller than that of the TMR devices, impedance matching of the GMR devices with the circuit is much easier to achieve due to their significantly lower resistance [14]. Use of TMR devices for microwave sensing is discussed in the article "Electronic transport in magnetic tunnel junction: a discussion of the electron-magnon-photon coupling" by Hong Guo and Y. Xiao.

Recently, there has been a lot of industrial effort to develop STT-RAM due to its high recording density, fast write/read speed (a few ns), unlimited endurance,

Monika Arora <mmonika@sfu.ca>, Tommy Mckinnon, Brett Heinrich, and Erol Girt <egirt@sfu.ca>, Department of Physics, Simon Fraser University, Burnaby, BC V5A 1S6, Canada

and

Ciaran Fowley, Ewa Kowalska, Volker Sluka, and Alina Maria Deac, Helmholtz-Zentrum Dresden-Rossendorf, Institute of Ion Beam Physics and Materials Research, Bautzner Landstrasse 400, 01328 Dresden, Germany

excellent scalability and potential of low power consumption [15]. One of the main difficulties in achieving this goal is that, the critical current density needed to reorient the magnetization is at present too high. For this reason, finding ways to minimize the critical current is the focus of intense research in both industrial and academic circles. In July 2015, Avalanche technology has announced the availability of its high-speed, non-volatile, 32/64Mbit STT-RAM magnetic memory [16]. Other companies working on STT-RAM include Everspin, IBM, Intel, IMEC, FUJITSU, GRANDIS, Hynix, Crocus Technology [17], and Spin Transfer Technologies [18,19].

In the macrospin approximation, the critical current required for spin-transfer reversal from P to AP and from AP to P state is given by [20]

$$I_c = -\left(\frac{2e}{\hbar}\right)\frac{\alpha M_s V_{FL}}{g(\theta)p}H_{eff} \qquad (1)$$

where M_s, α, and V_{FL} are the saturation magnetization, intrinsic Gilbert damping constant, and volume of the FL, respectively, p is the spin polarization of the current collinear with the RL magnetization, and $g(\theta)$ is a pre-factor depending on the relative angle between the RL and the FL. The effective field acting on the perpendicularly magnetized FL, $H_{eff} = \mp H_k \pm 4\pi M_s + H_{app} + H_{dip}$, has contributions from magnetic anisotropy field H_k, demagnetizing field $4\pi M_s$, applied field H_{app}, and the dipolar field from the reference layer H_{dip}.

In this paper, we have designed a RL having a synthetic antiferromagnet (SAF) structure to minimize the dipolar interaction, H_{dip}, between the RL and the FL and hence reduce H_{eff}. We are not aware of any investigations of devices with SAF layer consisting solely of Co/Ni multilayers. Most research to date has used a combination of Co/Pd, Co/Pt, Co/Ni and CoFe layers in SAF to increase the anisotropy [20–23]. I_c decreases in FL's with perpendicular magnetic anisotropy [24]. To minimize I_c we a used FL with a Co/Ni multilayer structure. Co/Ni multilayers have perpendicular anisotropy, low damping α, and high spin polarization p [24,25], which from Equation 1 are desirable for low I_c.

EXPERIMENTAL DETAILS

The magnetic multilayer films are deposited on Si(001) wafers by magnetron sputtering in a high vacuum deposition system with a base pressure of 7×10^{-8} Torr. The Si wafers are covered with a 100 nm SiO_2 layer to electrically isolate the wafer and metallic films. The sputtering parameters and the thicknesses of the individual layers are varied to optimize the magnetic properties of the (111) textured SAF/Cu/FL multilayer film structures. The SAF consists of two FM layers, FM1 and FM2, antiferromagnetically coupled across a Ru spacer layer of thickness 0.4 nm. FM1 is composed of 4 × [Co(0.2)/Ni(0.6)]/Co(0.4), FM2 is Co(0.4)/3 × [Ni(0.6)/Co(0.2)]/Ni(0.6)/Co(0.6), and the FL is 4 × [Co(0.2)/Ni(0.6)] (thicknesses are in nm). 3 nm of Cu is deposited as a spacer to decouple the SAF and the FL. To maximize the GMR effect in our structures, a thin Co layer is deposited on both sides of the Cu spacer layer. Ta(3 nm)/Cu(30 nm) are used as a bottom contact. The Ta/Cu bilayer structure also helps set up the (111) growth orientation for Co/Ni multilayers. For corrosion protection, the sample is covered by Ta(3 nm)/Ru(7 nm). The full STT MRAM structure is shown in Fig. 1a.

The sputtered films are cleaned in an ultrasonic acetone wash followed by isopropanol rinse then blown dry in N_2. The films are coated with a bilayer of photoresist (PR) LOL2000 (200 nm) and S1813 (1.3 μm) using a vacuum spin coater. The substrate is baked to drive out the excess solvent from the PRs. LOL 2000 is not UV sensitive and its role is to help complete liftoff of S1813. The sample with a photomask (Fig. 1a) is then loaded into the UV exposure tool and exposed. The films are developed in MF-319 and rinsed in de-ionised water. The areas not protected by the PRs are etched until the Si/SiO_2 substrate in an ion-milling tool using Ar^+ ions. SiO (70nm) is deposited by electron beam evaporation to fill up the etched portion of the structure and electrically isolate the individual devices. Samples were soaked in 1165 remover (NMP-based) and placed in an ultrasonic bath to liftoff the unwanted photoresist. A single patterned device image taken by an optical microscope is shown in Fig. 1b.

After cleaning the samples, a negative photoresist maN-2403 (300 nm) is used to coat the patterned films. E-beam lithography (EBL) is used to expose the wide side contact pads (200 × 50 μm) of H-shaped devices and the central circular area of diameter 200 nm Fig. 1c. Any unexposed resist is removed with maD-525 developer. The sample is then etched using Ar^+ ions until the Cu bottom layer, used as an electrical contact between the contact pads and the nanopillar. A 40 nm layer of SiO is deposited by thermal evaporation. This is shown in Fig. 1d, where the inset figure shows the 3D structure of the nanopillar. Acetone and 1165 are again used for PRs liftoff.

We again spin coat the bilayer of PRs on the top of the sample surface. UV light is used to expose the wide contact pads of the H device and the top contact area for the 200 nm nanopillar between the contact pads. The developed pattern is shown in Fig. 1e, where the olive green area represent the PRs. The device structure obtained after the deposition of Cr(5nm)/Au(125nm) layers on the top of sample surface and photoresist liftoff is presented in Fig. 1f (cross section).

Resistance of the nanopillar is measured using standard microwave probes. The current direction was set so that for positive current, electrons flow from SAF to FL. The probe station was capable of applying over 1 T field normal to the film surface.

A memory cell of a STT-RAM is composed of a GMR (or TMR) structure device, a transistor, a word line (WL), a bit line (BL), and a source line (SL) as shown in the Fig. 2. The BL and

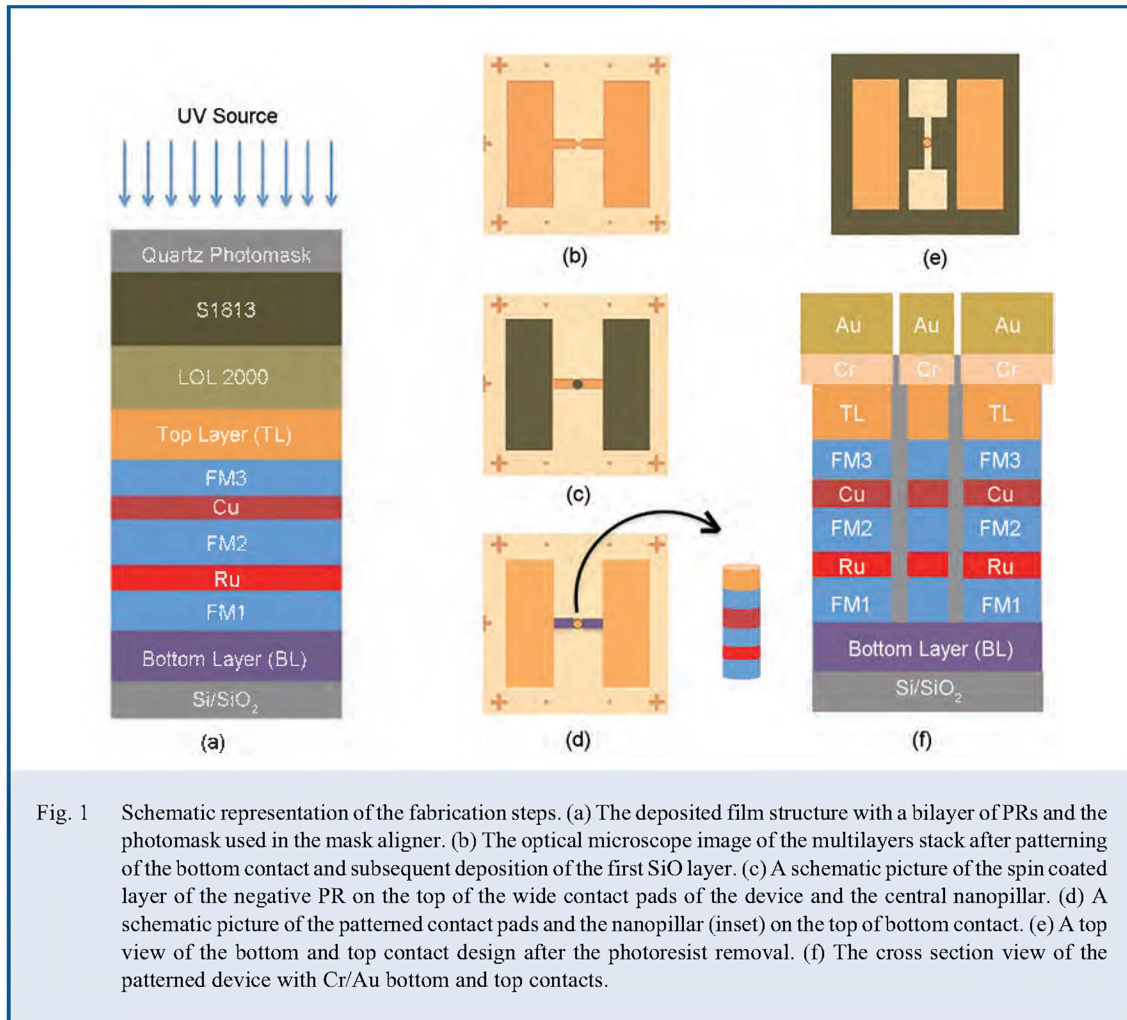

Fig. 1 Schematic representation of the fabrication steps. (a) The deposited film structure with a bilayer of PRs and the photomask used in the mask aligner. (b) The optical microscope image of the multilayers stack after patterning of the bottom contact and subsequent deposition of the first SiO layer. (c) A schematic picture of the spin coated layer of the negative PR on the top of the wide contact pads of the device and the central nanopillar. (d) A schematic picture of the patterned contact pads and the nanopillar (inset) on the top of bottom contact. (e) A top view of the bottom and top contact design after the photoresist removal. (f) The cross section view of the patterned device with Cr/Au bottom and top contacts.

WL are orthogonal to each other and this is indicated by the " × " sign. Each GMR device in a memory cell is connected in series to a transistor that controls the magnitude of current that passes through the GMR/TMR device. The transistor is controlled by the WL voltage that is adjusted for both read and write opretations so that a current can pass through the transistor. During a read operation a small voltage difference is applied between the BL and SL. This voltage difference causes a current density that is significantly lower than that required for reversal of the free layer to flow through the GMR/TMR device. The magnitude of current depends on the relative orientation of the magnetic layers in the GMR/TMR device: a parallel alignment corresponds to low resistance and large current (a "0" state), and an antiparallel alignment to high resistance and low current (a "1" state). During a write operation a large voltage difference is applied between the BL and SL to generate a current density large enough to reverse the direction of the magnetization of the FL. The torque on the magnetic moment of the FL is proportional to the

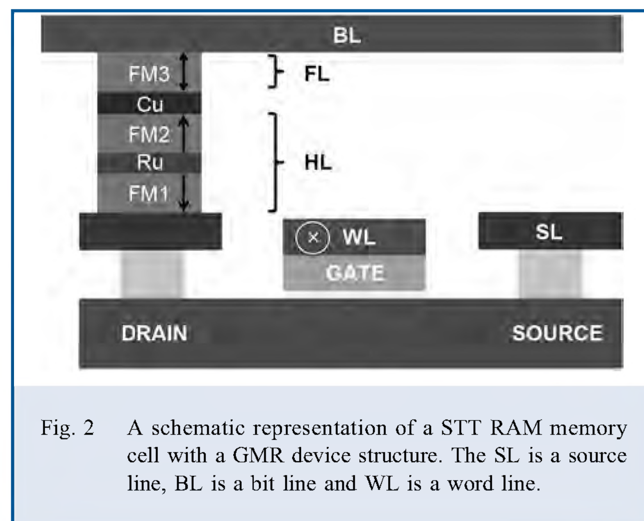

Fig. 2 A schematic representation of a STT RAM memory cell with a GMR device structure. The SL is a source line, BL is a bit line and WL is a word line.

current density flowing through the multilayer, and it changes sign when the current is reversed. Therefore, the magnetization of the FL can be reversed either parallel or antiparallel, with respect to HL, by changing the current direction from BL to SL.

RESULTS AND DISCUSSION

Magnetic measurements are performed on the continuous film before patterning. The measurements revealed perpendicular magnetic anisotropy ($2K_u/M_s > 4\pi M_s$, for $4 \times$[Co/Ni], a uniaxial anisotropy constant $K_u = 3.5 \times 10^5$ J/m^3, and a magnetic polarization $\mu_0 M_s = 0.7$ T) of each FM layer, and no coupling between SAF and FL. The measured coercivity, $\mu_0 H_c$, of the SAF and the FL in the continuous films is 0.23 T and 0.018 T, respectively.

The dc-resistance of a circular nanopillar of diameter 200 nm as a function of the applied field perpendicular to the surface of substrate is shown in Fig. 3. In the measurements the applied current is kept constant and equal to 0.5 mA. The direction of the magnetic moment in FM1, FM2 and FL varies with the applied field and is represented by arrows; the bottom arrow represents FM1, middle FM2 and top FL. At positive saturation field, the direction of magnetic moments of all the FM layers in the structure are parallel to the direction of the applied field, corresponding to a state of low resistance. As the field is reduced, the magnetic moment of FM1 reverses due to the antiferromagnetic exchange coupling between FM1 and FM2. Since FM1 and FM2 have the same film structure (Co/Ni multilayers) their magnetic anisotropy is similar. However, the Zeeman energy of FM1 is smaller than that of FM2 because the magnetization of FM1 is smaller than that of FM2. For this reason, the magnetic moment of FM1 in the SAF reverses first. The change from the parallel to antiparallel alignment between the magnetic moments of FM1 and FM2 in the SAF results in a slight increase in resistance.

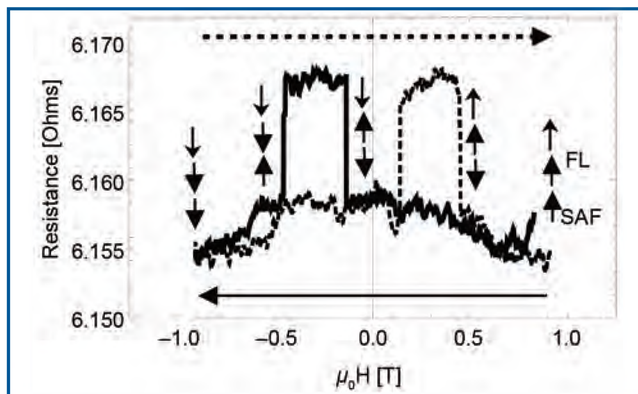

Fig. 3 R_{dc} measurement of the nanopillars as a function of the applied magnetic field. The vertical arrows represent the directions of the magnetic moments of FM1 (bottom arrow), FM2 (middle arrow) and FL (top arrow). The solid line represents the resistance measurements when the field sweeps from 0.9 T to -0.9 T and the dotted line represents the change in resistance when the field sweeps from -0.9 T to 0.9 T.

Further reduction of the applied magnetic field causes the reversal of the magnetic moment in FL at $\mu_0 H = -0.13$ T. At this field, alignment between the magnetic moments of the adjacent magnetic layers are antiparallel (both FM1 and FM2 are in the AP state, and FM2 and the FL are in the AP state) and hence resistance of the nanopillar increases to its highest value. The orientation of magnetic moments in the FM layers is unchanged from $\mu_0 H = -0.13$ to -0.49 T. At $\mu_0 H = -0.49$ T both magnetic layers in SAF (FM1 and FM2) simultaneously rotate. This sets the magnetic moment of the FL parallel to that of of FM2 resulting in a decrease of the nanopillar resistance. Even at this field the antiferromagnetic coupling across Ru is strong enough to ensure that mutual alignment between magnetic moments of FM1 and FM2 stays antiparallel. At negative saturation field, the magnetic moments of all the FM layers are aligned with the applied field, corresponding again to a state with the lowest resistance. The same trend is observed when the applied field sweeps from the negative saturation ($\mu_0 H = -0.8$ T) to the positive ($\mu_0 H = 0.8$ T).

The change in resistance due to the transition from the parallel to antiparallel alignment between the magnetic moments of FM1 and FM2 (Co/Ru/Co at ± 0.62 T) is about two and a half times smaller than the change in resistance due to the transition from the parallel to antiparallel alignment between the magnetic moments of FM2 and FL (Co/Cu/Co at ± 0.13 T and ± 0.49 T). This is due to the possible inter-diffusion of Co and Ru interfaces [26] and also due to a small difference between the spin-polarized density of states at the Fermi level [27]. The R_{dc} measurements are repeated for different values of applied current and it is observed that the coercive field of both the SAF and FL in the patterned nanopillars increases as compared to the continuous films, with the coercivity field of the SAF reaching $\mu_0 H_c = 0.49$ T and that of the FL $\mu_0 H_c = 0.098$ T. The increase of the coercivity field in both SAF and FL in nanopillars is due to size effects. In large magnetic structures, a defect or non-uniformity can act as a centre for a magnetic domain nucleation that causes the magnetization reversal at magnetic fields several orders of magnitude smaller than $2 K_u/M_s$ (where K_u is the magnetic anisotropy energy and M_s is the saturation magnetization of the magnetic structure). In *nm* -size magnetic structures much larger magnetic fields are required to nucleate a magnetic domain and cause the magnetization reversal [28,29] since the energy term due to the direct exchange interaction is dominant in *nm* -size structures.

The resistance as a function of d.c. current, measured at zero applied field, is shown in Fig. 4. The critical current, I_c, required to reverse the magnetization of FL from parallel to

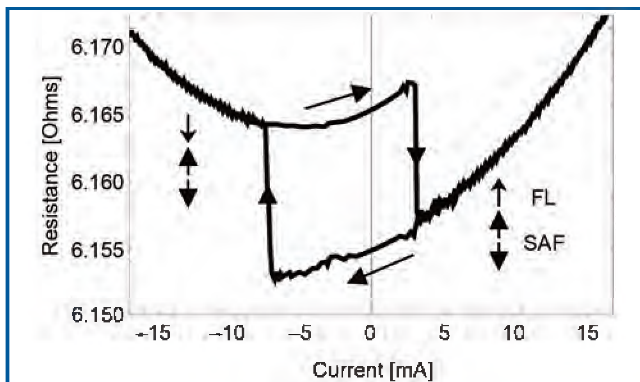

Fig. 4 Resistance measurement of the nanopillar as function of the applied dc current at a zero applied magnetic field. The arrows represent the directions of the magnetizations of FM1 (bottom arrow), FM2 (middle arrow) and FL (top arrow). The offset in resistance at 0 mA is due to the infinite resistance at zero current.

antiparallel alignment is $I_c = 6.6$ mA and from antiparallel to parallel is $I_c = 3$ mA.

The efficiency of current induced magnetization reversal of the FL can be determined from the expression $I_c/(V_{FL}H_c)$, where V_{FL} and H_c are the volume and coercivity of the FL, respectively. In our nanopillars $V_{FL} = 1.01 \times 10^{-22}$ m^3 and $H_c = 0.098$ T resulting in $I_c/(V_{FL}H_c)$ is 6.7×10^{20} A/T m^3. This is almost twice as efficient a current-induced magnetization reversal of FL than previous report for the devices with a SAF reference layer [20]. To decrease I_c, damping of the FL has to be minimized as shown in Equation 1. In previous study [20] FL was designed using both Co/Ni and Co/Pd multilayers. Co/Pd multilayers have higher damping than Co/Ni multilayers [30–32]. We further reduced damping in our Co/Ni multilayers by increasing the Co to Ni thickness ratio as suggested by Shaw *et al.* [33] and Mizukami *et al.* [34]. This can explain the higher efficiency of the spin transfer torque in our nanopillars.

CONCLUSION

We investigate current-induced magnetization reversal in perpendicularly-magnetized 200 nm diameter circular nanopillars with a unique magnetic layer design: a Co/Ni multilayer free layer (FL) and a synthetic antiferromagnet (SAF) reference layer. In our design, the dipolar field acting on FL is only 0.038 T, more than two times smaller than reported in devices with a single ferromagnetic reference layer [24]. In our devices the current-induced magnetization reversal of FL is almost twice as efficient as reported for the devices with a SAF reference layer [20]. This is attributed to a low damping design of our FL.

ACKNOWLEDGEMENTS

Financial support for this project was provided by the Natural Sciences and Engineering Research Council of Canada (NSERC).

REFERENCES

1. V. Turner, J. Gantz, D. Reinsel, and S. Minton, “The digital universe of opportunities: Rich data and the increasing value of the internet of things”, *International Data Corporation, White Paper* (2014).
2. J.J. Yang, D.B. Strukov, and D.R. Stewart, “Memristive devices for computing”, *Nature nanotechnology*, **8**, 13–24 (2013).
3. E. Kultursay, M. Kandemir, A. Sivasubramaniam, and O. Mutlu, “Evaluating STT-RAM as an energy-efficient main memory alternative”, *2013 IEEE International Symposium on Performance Analysis of Systems and Software (ISPASS)*, IEEE, 2013, pp. 256–267.
4. D. Bohn, *The Verge* (2015).
5. D. Ralph and M. Stiles, “Spin transfer torques”, *Journal of Magnetism and Magnetic Materials*, **320**, 1190–1216 (2008).
6. J. Slonczewski, “Current-driven excitation of magnetic multilayers”, *Journal of Magnetism and Magnetic Materials*, **159**, L1–L7 (1996).
7. M.N. Baibich, J.M. Broto, A. Fert, F.N. Van Dau, and F. Petroff, “Giant Magnetoresistance of (001)Fe/(001)Cr Magnetic Superlattices”, *Physical Review Letters*, **61**, 2472–2475 (1988).
8. G. Binasch, P. Grünberg, F. Saurenbach, and W. Zinn, “Enhanced magnetoresistance in layered magnetic structures with antiferromagnetic interlayer exchange”, *Physical Review B*, **39**, 4828–4830 (1989).
9. M. Julliere, “Tunneling between ferromagnetic films”, *Physics Letters A*, **54**, 225–226 (1975).
10. J. Akerman, “APPLIED PHYSICS: Toward a Universal Memory”, *Science*, **308**, 508–510 (2005).
11. A.V. Khvalkovskiy, D. Apalkov, S. Watts, R. Chepulskii, R.S. Beach, A. Ong, X. Tang, A. Driskill Smith, W.H. Butler, P.B. Visscher, *et al.*, “Erratum: Basic principles of STT-MRAM cell operation in memory arrays”, *Journal of Physics D: Applied Physics*, **46**, 139601 (2013).
12. M. Tsoi, A.G.M. Jansen, J. Bass, W.C. Chiang, M. Seck, V. Tsoi, and P. Wyder, “Excitation of a Magnetic Multilayer by an Electric Current”, *Physical Review Letters*, **80**, 4281–4284 (1998).

13. J.E. Wegrowe, D. Kelly, Y. Jaccard, P. Guittienne, and J.P. Ansermet, "Current-induced magnetization reversal in magnetic nanowires", *Europhysics Letters (EPL)*, **45**, 626–632 (1999).
14. J. Katine and E.E. Fullerton, "Device implications of spin-transfer torques", *Journal of Magnetism and Magnetic Materials*, **320**, 1217–1226 (2008).
15. Y. Huai, "Spin-transfer torque MRAM (STT-MRAM): Challenges and prospects", *AAPPS Bulletin*, **18**, 33–40 (2008).
16. *Avalanche Samples Industry's First STT-MRAM Chips On 300MM Wafers Utilizing Advanced Perpendicular MTJ* (2015).
17. L. McHale, *Crocus Technology Enters STT Memory Race and Sets Industry Pace with New Prototype* (2009).
18. V. Chun, *Interview with Vincent Chun from Spin Transfer Technologies* (2008).
19. M. Companies, *MRAM-info Companies* (2012).
20. I. Tudosa, J.A. Katine, S. Mangin, and E.E. Fullerton, "Perpendicular spin-torque switching with a synthetic antiferromagnetic reference layer", *Applied Physics Letters*, **96**, 212504–3 (2010).
21. Y. Jiang, T. Nozaki, S. Abe, T. Ochiai, A. Hirohata, N. Tezuka, and K. Inomata, "Substantial reduction of critical current for magnetization switching in an exchange-biased spin valve", *Nature materials*, **3**, 361–364 (2004).
22. Y. Jiang, G.H. Yu, Y.B. Wang, J. Teng, T. Ochiai, N. Tezuka, and K. Inomata, "Spin transfer in antisymmetric exchange-biased spin-valves", *Applied Physics Letters*, **86**, 192515–3 (2005).
23. D.B. Gopman, D. Bedau, S. Mangin, E.E. Fullerton, J.a. Katine, and a.D. Kent, "Bimodal switching field distributions in all-perpendicular spin-valve nanopillars", *Journal of Applied Physics*, **115**, 17C707–3 (2014).
24. S. Mangin, D. Ravelosona, J.a. Katine, M.J. Carey, B.D. Terris, and E.E. Fullerton, "Current-induced magnetization reversal in nanopillars with perpendicular anisotropy", *Nature Materials*, **5**, 210–215 (2006).
25. H.S. Song, K.D. Lee, J.W. Sohn, S.H. Yang, S.S.P. Parkin, C.Y. You, and S.C. Shin, "Observation of the intrinsic Gilbert damping constant in Co/Ni multilayers independent of the stack number with perpendicular anisotropy", *Applied Physics Letters*, **102**, 102401–5 (2013).
26. S. Zoll, A. Dinia, J.P. Jay, C. Mény, G.Z. Pan, A. Michel, L.El Chahal, V. Pierron-Bohnes, P. Panissod and H.A.M.V. den Berg, "Influence of the growth technique on the coupling and magnetoresistance of Co/Ru sandwiches", *Phys. Rev. B*, **57**, 4842–4848 (1998).
27. T. Kai, Y. Ohashi, and K. Shiiki, "Study of giant magnetoresistance in Co/X superlattices (X = Cu, Ru, Rh and Pd) by first-principle band calculation", *Journal of magnetism and magnetic materials*, **183**, 292–298 (1998).
28. E.F. Kneller and F.E. Luborsky, "Particle Size Dependence of Coercivity and Remanence of Single-Domain Particles", *Journal of Applied Physics*, **34**, 656–658 (1963).
29. E. Girt, K. Krishnan, and G. Thomas, "Optimization of magnetic properties of nanostructured Nd-Fe-B: approaching ideal Stoner-Wohlfarth behaviour", *Scripta Materialia*, **44**, 1431–1435 (2001).
30. T. Kato, Y. Matsumoto, S. Kashima, S. Okamoto, N. Kikuchi, S. Iwata, O. Kitakami, and S. Tsunashima, "Perpendicular Anisotropy and Gilbert Damping in Sputtered Co/Pd Multilayers", *IEEE Transactions on Magnetics*, **48**, 3288–3291 (2012).
31. J.M. Shaw, H.T. Nembach, and T.J. Silva, "Determination of spin pumping as a source of linewidth in sputtered Co 90 Fe 10 /Pd multilayers by use of broadband ferromagnetic resonance spectroscopy", *Physical Review B*, **85**, 054412–10 (2012).
32. S. Pal, B. Rana, O. Hellwig, T. Thomson, and A. Barman, "Tunable magnonic frequency and damping in [Co/Pd][sub 8] multilayers with variable Co layer thickness", *Applied Physics Letters*, **98**, 082501–3 (2011).
33. J.M. Shaw, H.T. Nembach, and T.J. Silva, "Damping phenomena in Co90Fe10/Ni multilayers and alloys". *Applied Physics Letters*, **99**, 012503–3 (2011).
34. S. Mizukami, X. Zhang, T. Kubota, H. Naganuma, M. Oogane, Y. Ando, and T. Miyazaki, "Gilbert Damping in Ni/Co Multilayer Films Exhibiting Large Perpendicular Anisotropy", *Applied Physics Express*, **4**, 013005–3 (2011).